Computers & Geosciences 35 (2009) 1917–1924

Contents lists available at ScienceDirect

Computers & Geosciences

journal homepage: www.elsevier.com/locate/cageo

Spatial point pattern analysis applied to bubble nucleation in silicate melts ☆

Joanna Mongrain [a,*], Jessica F. Larsen [b]

[a] Petroleum Engineering Department, University of Alaska, Fairbanks, AK 99775, United States
[b] Geophysical Institute, University of Alaska, Fairbanks, AK 99775, United States

ARTICLE INFO

Article history:
Received 24 April 2008
Received in revised form
15 January 2009
Accepted 21 January 2009

Keywords:
Bubble
Spatial statistics
Spatstat
Nucleation
Experiments

ABSTRACT

Experimental bubble nucleation studies are used for determining the nucleation mechanism as a function of experimental conditions, the resulting bubble number density, and can also yield estimates of the melt-vapor surface tension. This provides important information on gas exsolution in silicate melts, which can be applied towards understanding magmatic degassing in volcanic conduits. At present, determination of nucleation processes in tiny experimental samples relies upon visual observations. To improve the characterization of the spatial distribution of bubbles, we present a new application of spatial point pattern analysis. This technique allows the quantitative description of the spatial distribution of nucleation sites and has the potential to distinguish between homogeneous, heterogeneous, and multiple nucleation events. Since point pattern analysis highlights clustering or spatial regularity among objects, it may improve our understanding of the melt structure underlying the spatial distribution of nucleation sites, as well as interactions between bubble populations resulting from different nucleation pulses within a single experimental sample.

1. Introduction

Spatial point pattern analysis is a powerful technique applied to datasets, which record the spatial location of objects observed within a certain region. It has been used across many disciplines studying the spatial distribution of objects such as trees (Cox, 1979), galaxies (Peebles, 1974), and neuron profiles in brains (Diggle et al., 1991).

We present the application of spatial point pattern analysis to bubble nucleation experiments performed in silicate melts decompressed and quenched from high pressures and temperatures. Through a quantitative description of the spatial distribution of bubbles there exists the potential to distinguish between homogeneous and heterogeneous nucleation mechanisms beyond simple visual observations (e.g., Hurwitz and Navon, 1994; Mangan and Sisson, 2000). This approach may also enable researchers to separate multiple nucleation events that occurred within one experiment. Since this technique highlights clustering or spatial regularity in nucleation sites it may prove useful in elucidating the underlying melt structure or point to the locations of sub-microscopic crystallites. The ability to make quantitative comparisons between and within samples, gives insights into the spatial controls on nucleation unattainable through any other current methods applicable to experimental samples.

2. Background

Classical nucleation theory describes the thermodynamics of fluid-phase separation, and is commonly applied to gas–vapor exsolution in silicate melts. Following Hurwitz and Navon (1994), the nucleation rate, J, at ΔP – the difference between the melt pressure and the internal pressure in the critical nucleus – can be calculated using Eq. (1) (e.g., Hirth et al., 1970)

$$J = J_0 \exp\left(-\frac{16\pi\sigma^3}{3kT\Delta P^2}\right) \quad (1)$$

where J_0 is a pre-exponential factor related to the concentration and molar volume of dissolved H_2O molecules in the melt, k is the Boltzmann constant, T is the temperature, and σ is the surface tension. Derivation of J_0 is detailed in Hurwitz and Navon (1994) and Toramaru (1989). According to the kinetic model of Kolmogorov–Johnson–Mehl–Avrami (Avrami, 1940; Johnson and Mehl, 1939; Kolmogorov, 1937), the nuclei result from random volatile fluctuations. Therefore, the spatial distribution of homogenously nucleated bubbles should approximate a spatially random Poisson distribution. In contrast, heterogeneous bubble nucleation may occur at much lower ΔP, because of the reduction in excess free energy associated with nucleation on a crystal surface (Hurwitz and Navon, 1994). In this case, the spatial arrangement of bubbles may be homogeneous or

☆ Code available from server at http://www.iamg.org/CGEditor/index.htm.

* Corresponding author. Tel.: +1 907 474 7574.
E-mail address: ffjcm1@uaf.edu (J. Mongrain).

0098-3004/$ - see front matter © 2009 Elsevier Ltd. All rights reserved.
doi:10.1016/j.cageo.2009.01.008

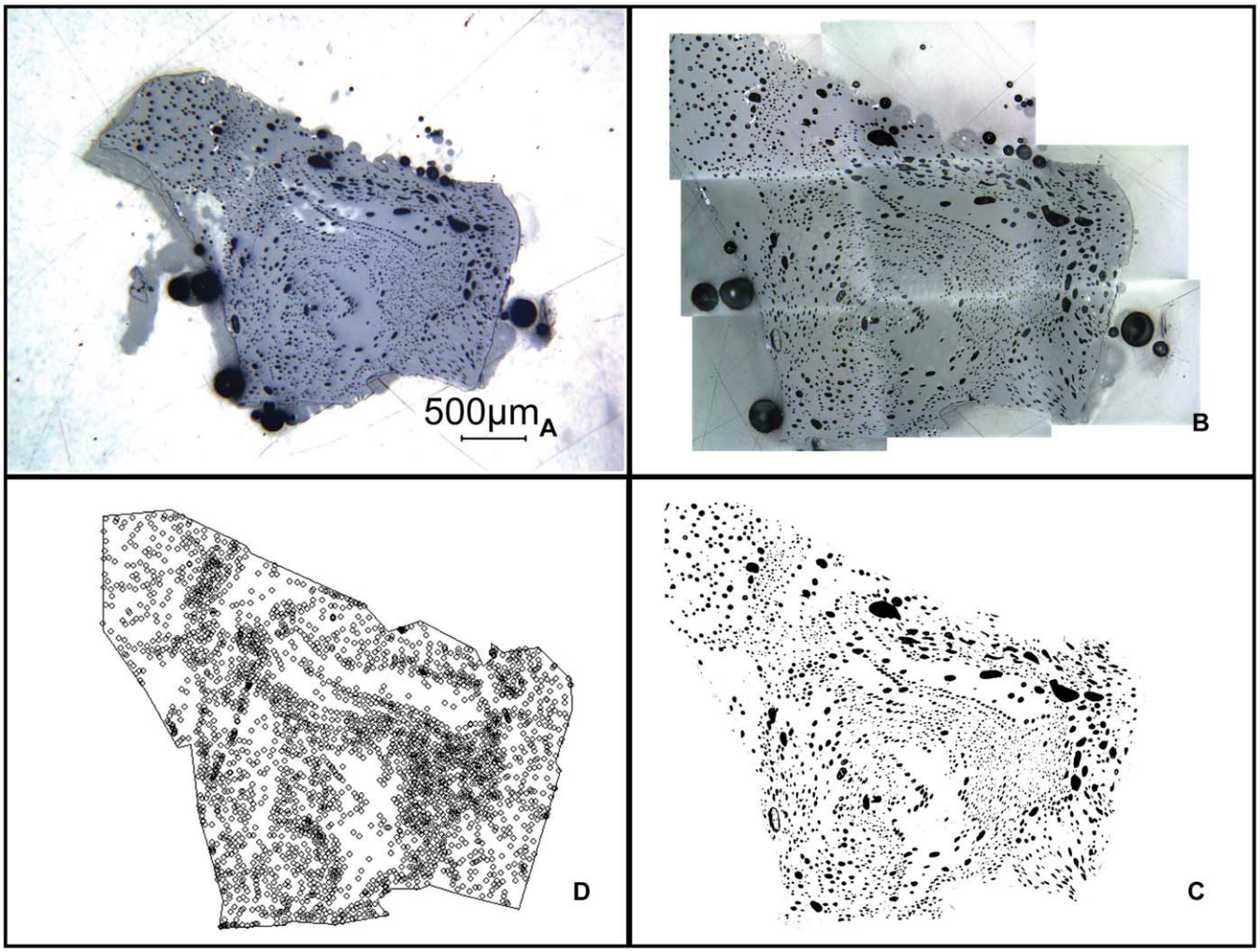

Fig. 1. Workflow illustration for creation of spatial point patterns from experimental nucleated samples. (A) Overview Photomicrograph. (B) Sample Photomontage. (C) Threshold Image. (D) Spatial Point Pattern.

heterogeneous and reflects the spatial distribution and number of crystals (Hurwitz and Navon, 1994; Mangan and Sisson, 2000; Cluzel et al., 2008).

3. Methods

3.1. Sample image preparation

To apply spatial statistics analyzes to experimental samples, a well-polished sample surface for high-quality photomicrographs are required. Thin sections of the experimental samples are prepared by embedding the samples in epoxy, mounting on microscope slides, and polishing finely. A series of photomicrographs are taken in reflected light of the finely polished sample in an overlapping grid fashion using a micrometer slide holder, ensuring that each photomicrograph overlaps its neighbor by 40%. The images in this study were taken at 100 × with a Leica DM LM/P petrographic light microscope and Leica DF320 digital camera with a 2.98 pixels /micron resolution. The images are then imported into Adobe Photoshop and a photomontage created using the photomerge function. This process recreates an image of the entire sample but at a higher resolution than would be allowed by using fewer images collected using a lower magnification.

3.2. Point pattern generation

The photomontage is imported into the ImageJ[1] and the global scale set to the correct pixel/micron ratio calibrated from the camera used to collect the photomicrographs. The perimeter of the sample can be traced using the multi-select tool and the coordinates of the perimeter exported as a text file. Using image thresholding to highlight the bubbles, the coordinates of the centroids of the bubbles intersecting the surface are determined by selecting *centroid* and *limit to threshold* in the Set Measurements menu and then selecting Analyze Particles. These can be exported as a text file from the Results and saved with the extension *.tab*. Depending on the image quality some manual thresholding may be required. Fig. 1 shows examples of a bubble nucleation experiment image, photomontage, thresholded image, and centroids analyzed by ImageJ plotted as a point pattern in panel D. The bubble centroid dataset is then imported into a suitable spatial analysis package for derivation of the spatial distribution functions.

[1] ImageJ. http://rsb.info.nih.gov/ij/.

3.3. Point pattern loading

Spatstat[2] is a package developed by Baddeley and Turner (2005) for the *R* statistical computing platform (R Development Core Team, 2007). *R* compiles and runs on UNIX, Windows and MacOS. Where other packages require the window to be of a regular shape, Spatstat is unique in the use of an arbitrary window. This allows analysis of the entire sample at once, which is a more rigorous statistical approach and particularly useful for examination of experimental samples where the nucleation pattern may differ between the edge and center of the sample. After installing the two packages, the bubble centroid point pattern dataset created in ImageJ is loaded into Spatstat for statistical analysis. The appendix contains detailed instructions for processing a bubble centroid point pattern along with a simple sample dataset and the corresponding generated plots.

To load the point pattern data (i.e., bubble centroids), open the R GUI and load the Spatstat package using the command *library*(*spatstat*). Set the working directory to the folder containing your point pattern files *File* > *Change dir*. The user should be aware that all commands are case sensitive.

Before importing the sample point patterns, a sample window must be created using the coordinates of the sample perimeter. To create the window object, *window*, use the command

$$window <- owin(poly = list(x = c(0.5,\ 1,\ 0.2, \ldots\ldots\ldots),\ y = c(0,\ 1,\ 2, \ldots\ldots)))$$

where the *x* and *y* coordinates are the exported sample perimeter coordinates. The sample point pattern is then imported and associated with this window.

To create the point pattern object, *Example*, using points collected in the file sites_example.tab, within the newly created window object, *window*, use the following command:

$$Example <- scanpp(\text{“}sites\_example.tab\text{”}, window, dir = \text{“”},\ header = FALSE, multitype = FALSE)$$

To check that the point pattern object, *Example*, reproduces the point pattern correctly use *plot*(*Example*) to generate a plot of the point pattern within its associated window (Fig. 1) and compare with the original photomontage, and threshold images. The orientation of the point pattern is a mirror image of the original photomicrograph due to differences in the point of origin location between ImageJ and Spatstat.

3.4. Spatial statistics

3.4.1. Point pattern summary

Spatstat provides a number of ways to observe and derive fundamental data from a point pattern containing experimental bubble centroids. The number of bubbles within the analytical window and the 2D bubble number density (the number of intersected bubbles per unit area) can be found using the function *summary*(*Example*). The spatial homogeneity of the point pattern can be assessed using a kernel smoothed intensity plot or shaded relief contour map image of bubble density across the surface of the sample. To generate this plot use the command below. The second parameter within the brackets is the kernel size, which is defined as the standard deviation of the Gaussian smoothing kernel. The computation is by Fast Fourier Transform (FFT) where the pixel resolution is defined by the parameter, dim*yx*.

$$plot(density.ppp(Example, 100, \mathrm{dim}yx = c(300, 300)))$$

[2] Spatstat. http://www.cran.rproject.org/src/contrib/Descriptions/spatstat.html.

Fig. 2B shows this plot function applied to rhyolite experiment RN1B, which underwent homogeneous bubble nucleation after large ΔP, demonstrating the variation in bubble number density across the surface of the sample. A plot of the bubble centroid locations can be created using *plot*(*Example*) and compared with the density plot (Fig. 2C).

Since bubbles nucleated around the edges of the sample may not be controlled by the same processes as bubbles in the center, we may wish to remove them to allow analysis of “internally” i.e., homogeneous; (Mangan and Sisson, 2000) nucleated bubbles only. This can be achieved in an objective manner using the following function, which reduces the window of analysis by a given distance:

$$new\_300 <- erode.owin(window, 300)$$

The subset of points from the previously defined point pattern, *Example*, falling within this window (new_300) can be expressed as a new point pattern object for separate analysis using the following function where the new window is defined within square brackets.

$$int\_300 <- Example[new\_300]$$

This allows statistical analysis for the whole sample and internal sections of the sample to be compared.

3.4.2. Point pattern analysis

Before describing the application of statistical spatial point pattern analysis, it is important to recognize two assumptions about the underlying point process. The process is stationary (invariant under translations) and isotropic (invariant under rotations). In addition, it is often assumed for planar sections that the statistical averages for the sample (i.e., multiple sections) as a whole can be expressed as the spatial average in just one. This allows statistical inference for the whole sample to proceed from a single section.

To aid in quantifying differences between samples, the observed spatial point patterns are usually compared to a reference model that corresponds to complete spatial randomness, the stationary Poisson Point Process. Point patterns can then be classified as being more aggregated/clustered or more regular than a distribution arising from a Poisson process with the same intensity, the number of events per unit area. Following from this, there are a number of useful distribution functions that can be derived from the point pattern of interest, and applied specifically to decipher bubble nucleation processes, as follows.

3.4.2.1. Nearest neighbor distribution function G(r). A simple description of the spatial distribution of the intersected bubbles is based on the measurement of the distance from the center of the intersection of a typical bubble to the center of its nearest neighbor. The nearest neighbor cumulative distribution $G(r)$ at a radius r is defined as follows, where $P()$ denotes probability.

$$G(r) = P(\text{distance from a typical point to the nearest point } of \text{ process} \leqslant r) \quad (2)$$

For the stationary Poisson point process of intensity λ, the G function $G_{Poiss}(r)$ is given by

$$G_{Poiss}(r) = 1 - e^{(-\lambda \pi r^2)} \quad (3)$$

Comparing $G(r)$ for the sample with $G_{Poiss}(r)$ highlights any clustering or spatial regularity in the intersected bubble population (e.g., Fig. 3). As $G(r)$ is a cumulative function, point patterns, which are more regularly spaced than the point pattern derived from a Poisson process should plot below $G_{Poiss}(r)$ whilst clustered

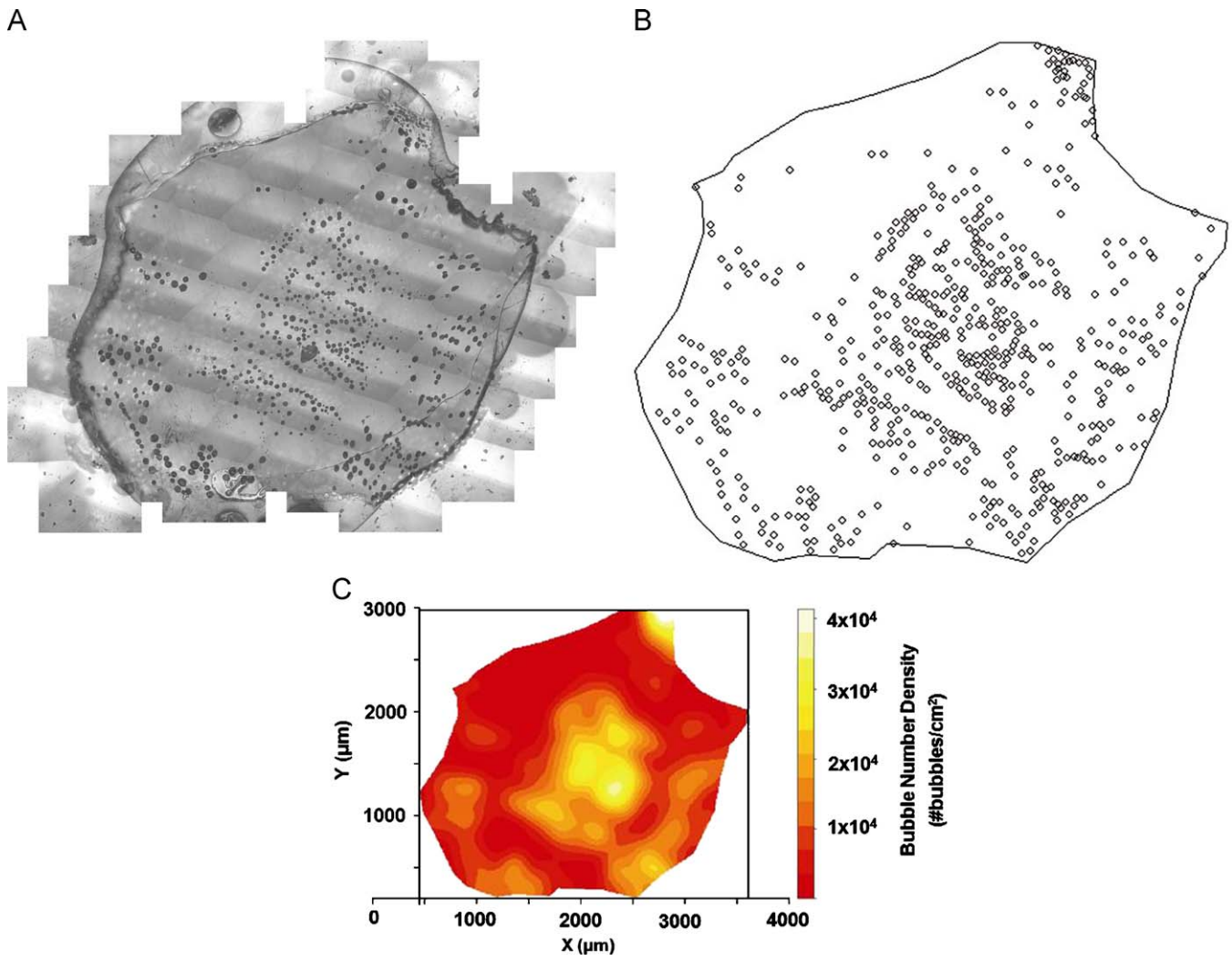

Fig. 2. Sample RN1B images. (A) Overview photomicrograph. (B) Spatial point pattern. (C) Bubble number density plot, kernel size is 100.

patterns will plot above. Calculations of $G(r)$ can be affected by biases introduced through edge effects. Spatstat corrects for this bias using either the Kaplan–Meier or a reduced sample estimator. The reduced sample estimator excludes points that lie within a certain distance from the sample edges. The Kaplan–Meier estimator, detailed in Baddeley (1998), utilizes $G(r)$ to correct for edge effects.

To create the object *G_Example*, which is a function value object containing the estimated values of $G(r)$ for the point pattern, *Example*, use the *Gest* command as follows:

G_Example $<-$ *Gest*(*Example*)

3.4.2.2. Ripley's K-function. Ripley's *K*-function $K(r)$ or the reduced second moment distribution of a point process is a good first-order test of homogeneity highlighting over what length scale the point pattern can be said to be homogeneous, where $E()$ is the estimator function

$$K(r) = \frac{E((\text{Number of points within } r \text{ of typical point}) - 1)}{\lambda} \quad (4)$$

For the Poisson process, which has an intensity, λ,

$$K_{Poiss}(r) = \pi r^2 \quad (5)$$

A commonly used transformation of $K(r)$ is the *L*-function given by Eq. (6), which transforms the Poisson *K*-function to the straight line $L_{Poiss}(r) = r$, making visual assessment of the graph much easier (e.g., Fig. 3). Clustered patterns will plot above $L_{Poiss}(r)$. Regular patterns will plot below $L_{Poiss}(r)$ for some minimum *r*. The command *Lest* will generate $L(r)$ for a point pattern.

$$L(r) = \sqrt{\frac{K(r)}{\pi}} \quad (6)$$

Standard errors for the summary statistics cannot be calculated in Spatstat (Baddeley and Turner, 2005). Whilst this is a weakness of the approach, there are currently no simple expressions in the literature for real datasets, particularly with irregular shaped windows. Acknowledgement of this drawback should not restrict the use of Spatstat in analyzing bubble nucleation datasets.

3.4.2.3. Choice of reference model. A 2D Poisson point process generates a completely spatially random (CSR) point pattern of defined intensity, λ. The CSR model is commonly used in exploratory spatial analysis as a reference model. A common reference model eases the comparison of differing point patterns as the effect of the intensity is removed. Therefore, point patterns derived from processes, which have the same underlying mechanism but operate on different scales can be recognized. For this

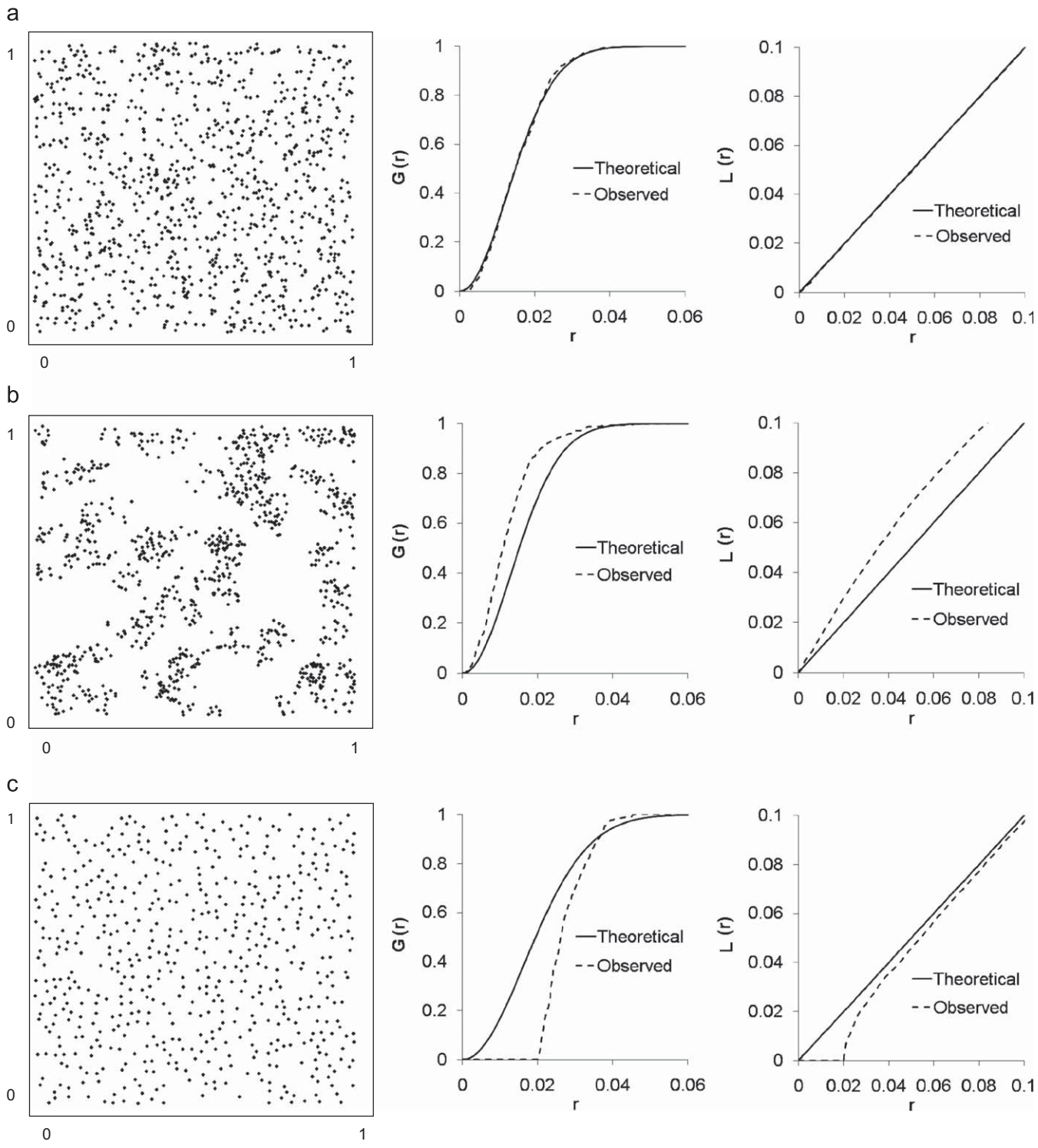

Fig. 3. Three example point patterns illustrating random, clustered, and ordered patterns and summary statistics $L(r)$ and $G(r)$ for each. Point patterns were generated within Spatstat where (a) is generated from a Complete Spatial Randomness (CSR) model, (b) is generated from a Matern Cluster model and (c) is generated from a Matern II model (ordered).

reason, the Poisson model was chosen as the base reference model allowing us to focus on differences in nucleation mechanism rather than sample intensity. A case may also be made that for our samples, the CSR is particularly appropriate. Classical nucleation theory tells us that the 3D distribution of homogeneously nucleated bubbles assuming no coalescence or bubble growth follow a Poisson distribution. Our analyzed samples differ in that they are 2D sections of the 3D distribution and that bubble growth and potentially coalescence has occurred. Should we expect that the spatial pattern of intersected bubbles in 2D sections of a homogeneously nucleated bubble population should also follow a Poisson distribution? To address this issue, Jerram et al. (1996) performed a large study on 2D sections through a cube filled with randomly packed spheres. Taking a range of packing volumes,

they calculated R, the ratio of the mean centroid-to-centroid distance, r_A, to the predicted mean nearest neighbor distance for a random distribution of points, r_E, i.e., Poisson. They found that as the percentage volume of spheres decreased, R approached 1. At 15% sphere volume, $R = 1.2$, at 5% sphere volume $R \sim 1.1$. In other words, as the percentage volume of the spheres decreased, the mean centroid-to-centroid distance approached that expected for a random distribution of points with the same areal intensity. The porosities in our samples are low 6.46(2.65) vol% for RN1B and 12.01(2.67) vol% for 79VB2C, where the number in brackets are standard deviations. Experimental bubble studies (Burgisser and Gardner, 2004; Larsen et al., 2004; Mongrain and Larsen, 2008) suggest that coalescence is limited at these porosities. We therefore expect that if the bubble centers exhibit a 3D Poisson distribution in 3D this will be expressed in 2D, using the 2D bubble number density, as close to a random distribution. Large deviations from the CSR curve will indicate clustering/spatial regularity.

An advanced analysis would take into account the finite size of the bubbles, which results in a minimum separation distance between bubble centers. The effect of finite bubble size has a clear effect on the summary statistics $G(r)$ and $L(r)$. In both cases, the effect of the finite bubble size will be to depress $G(r)$ and $L(r)$ below the respective Poisson curves for small values of r. If we know the true bubble sizes, we can modify our approach. In this study, we used point patterns derived from a Matern II model as an additional comparison curve. In this model, the points of a homogeneous Poisson process are marked by 'arrival times', which are independent and uniformly distributed. Any point that lies closer than a distance, r (set to the smallest measured true bubble diameter), from another point that has an earlier arrival time, is deleted. In this way, we can generate a point pattern for comparison with our samples that accounts for the minimum interbubble distance but assumes that the bubbles are otherwise randomly distributed.

To create the object *rmII* for a point pattern with intensity, kappa, with an inhibition distance of r, use the following command line

$$rmII <- r\ MaternII(kappa, r, win = owin(c(o, 1, \ldots), c(o, 1, \ldots))) \quad (7)$$

3.4.2.4. Data export. To export the distribution data to a table, which can be opened in a plotting program such as excel, use the following

write.table(*F_Example*, *file* = "*F_Example.txt*", *append* = *FALSE*, *quote* = *TRUE*, *sep* = " ", *row.names* = *TRUE*, *col.names* = *TRUE*)

4. Application of spatstat to bubble nucleation experiments

4.1. Homogeneous nucleation: sample RN1B

Sample RN1B was conducted to replicate homogeneous bubble nucleation in rhyolite melt under similar conditions to those employed by Mangan and Sisson (2000). It shows two populations of bubbles: one nucleated around the edges and the other forming a "cloud" with high bubble number density in the center (Fig. 2A). Fig. 2C shows a contoured density map of the spatial point pattern (Fig. 2B) derived from the bubble centroids from a thin section of sample RN1B. The bubble number density varies by an order of magnitude across the intersected sample from $\sim 5 \times 10^3$ to $\sim 4 \times 10^4$ bubbles cm^{-2}, with the highest bubble number density in the center of the sample surrounded by a region containing the lowest bubble number densities (Fig. 2C). Fig. 2B confirms that a high bubble number density is found in the center of the sample and is surrounded by an essentially bubble free area. The sample edges have intermediate bubble number densities.

The spatial statistics functions $G(r)$ and $L(r)$ are shown in Figs. 4 and 5, compared to the distribution expected from a Poisson process, $G_{Poiss}(r)$ and $L_{Poiss}(r)$, with the same average intensity and a Matern II model with a minimum spacing of 16 μm. In Fig. 4, $G(r)$, for the sample plots below $G_{Poiss}(r)$ for $r < \sim 40$ μm but shows a similar distribution to the Matern II model for $r < \sim 35$ μm. Using the isotropic corrected method, $L(r)$ plots below $L_{Poiss}(r)$ for $r < 36$ μm with $L(r) = 0$ for $r < 18$ μm and above $L_{Poiss}(r)$ for values of $r > 36$ μm. The Matern II model distribution is again similar for $r < \sim 35$ μm. Performing similar modeling using a subset of bubbles in a window reduced by 500 μm from the original

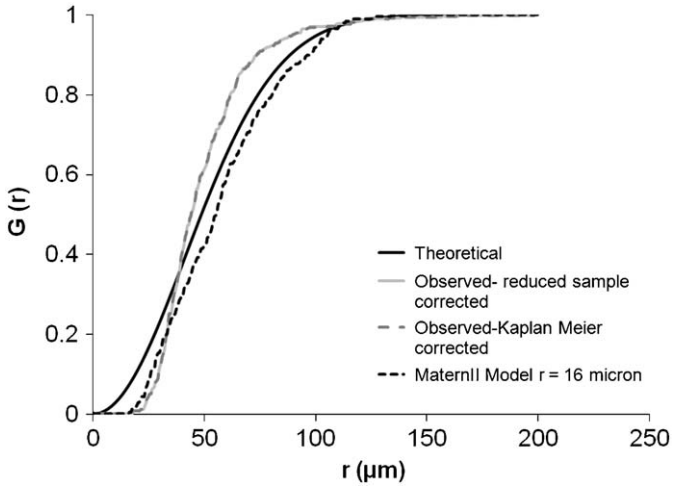

Fig. 4. $G(r)$ vs. $G_{Poiss}(r)$ for sample R1NB. Edge corrected nearest neighbor cumulative distributions, $G(r)$, for sample RN1B plotted against expected distribution from a Poisson distributed point pattern $G_{Poiss}(r)$ of same intensity. Solid black line is $G_{Poiss}(r)$, solid light grey line is $G(r)$ after reduced sample correction, and dashed dark grey line is $G(r)$ after Kaplan–Meier correction. Dashed black line is distribution derived from a Matern II model with minimum separation of 16 μm.

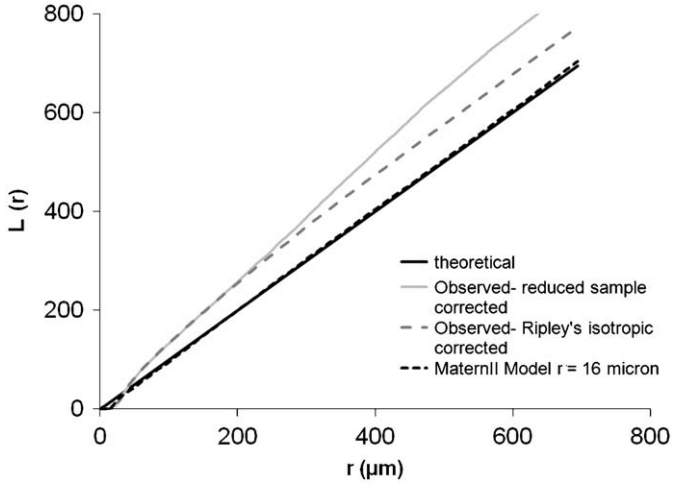

Fig. 5. $L(r)$ vs. $L_{Poiss}(r)$ for sample RN1B. Edge corrected nearest neighbor cumulative distributions, $L(r)$, for sample RN1B plotted against expected distribution from a Poisson distributed point pattern $L_{Poiss}(r)$ of same intensity. Solid black line is $G_{Poiss}(r)$, solid light grey line is $G(r)$ after reduced sample correction, and dashed dark grey line is $G(r)$ after Kaplan–Meier correction. Dashed black line is distribution derived from a Matern II model with minimum separation of 16 μm.

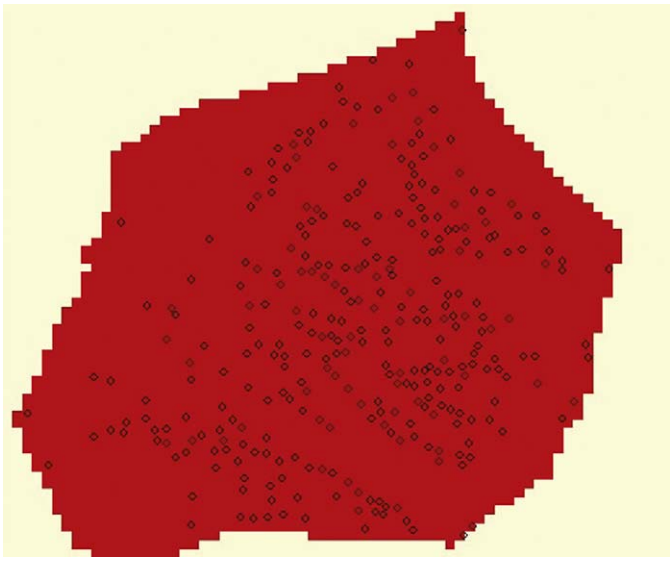

Fig. 6. Plot showing subset of points for sample RN1B within window reduced by 500 μm.

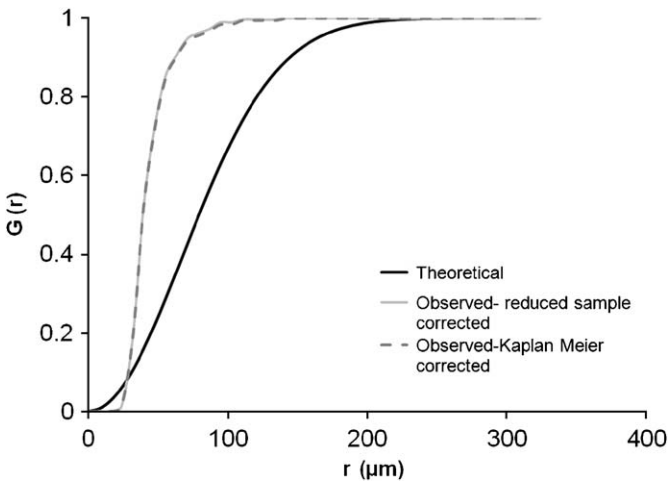

Fig. 7. $G(r)$ vs. $G_{Poiss}(r)$ for subsets of sample RN1B derived from 500 μm reduction in window size. Edge corrected nearest neighbor cumulative distributions, $G(r)$, for subsets of sample RN1B derived from 500 μm reduction in window size plotted against expected distribution from a Poisson distributed point pattern $G_{Poiss}(r)$ with same average intensity of entire sample. Solid black line is $G_{Poiss}(r)$, solid light grey line is $G(r)$ after reduced sample correction, and dashed dark grey line is $G(r)$ after Kaplan–Meier correction.

(Fig. 6) results in dramatically different calculated $G(r)$ (Fig. 7). Here, $G(r)$ plots dramatically above $G_{Poiss}(r)$ for all $r > 24$ μm with 95% of nearest neighbor distances occurring at less than 80 μm compared with less than 166 μm for $G_{Poiss}(r)$.

Based on visual observations (Mangan and Sisson, 2000), RN1B underwent homogeneous bubble nucleation, producing the high bubble number density in the sample center. The bubbles at the sample edge are assumed to have nucleated heterogeneously and the two bubble populations are considered to be independent. Spatstat allows further details to emerge beyond those derived from visual recognition alone. For a clustered arrangement where the distance between points is shorter than would be expected from a Poisson distribution with the same overall intensity, $G(r)$ and $L(r)$ are expected to plot above $G_{Poiss}(r)$ and $L_{Poiss}(r)$, respectively. Analyzing the whole sample in RN1B results in the $G(r)$ curve (Fig. 4) crossing where part of the bubble population can be classified as being more clustered and the other as being more regularly spaced. In this case, we can clearly see that the internal and edge bubbles represent two independent bubble populations and that a description of the sample is not well served by using a single point process model.

Considering only the internally nucleated bubbles (Fig. 7), $G(r)$ plots above $G_{Poiss}(r)$, indicating that the bubbles are more clustered than would be expected from a Poisson distribution with the same average intensity. However, the steep slope of $G(r)$, 85% of the intersected bubbles have a nearest neighbor in the range 25–55 μm, also indicates that the bubbles are somewhat regularly spaced within the cluster. This correlates well with the observations of spatial regularity made by Mourtada-Bonnefoi and Laporte (2004) from similar nucleation experiments. Interestingly, we should not expect such spatial regularity in a theoretical homogeneously nucleated melt, since the spatial pattern should plot closer to the completely spatially random Poisson distribution. The distinct signature in $G(r)$ of the internal nucleated bubbles in sample RN1B may be used to quantify "homogeneous" nucleation beyond simple visual recognition.

4.2. Heterogeneous nucleation: sample 79VB2C

The spatial bubble distribution in Sample 79VB2C is complex (Fig. 1). The sample is not considered to have undergone a simple homogeneous nucleation step. The complex spatial point pattern may derive from multiple nucleation events, which could be homogeneous and/or heterogeneous.

Fig. 8 shows a contoured density map of the spatial point pattern derived from sample 79VB2C. The bubble number density varies by an order of magnitude across the sample surface, from $\sim 2 \times 10^4$ to $\sim 1.4 \times 10^5$ bubbles cm^{-2}, yet without clear organization between separate edge and interior bubble populations as in RN1B. $G(r)$ for sample 79VB2C is shown in Fig. 9, compared to the distribution expected from a Poisson process, $G_{Poiss}(r)$, with the same average intensity and a Matern II model with a minimum spacing of 5 μm. The observed $G(r)$ is less than $G_{Poiss}(r)$ for all r indicating that the points in general are more regularly spaced that would be expected from a Poisson distribution. In Fig. 9, plots of $G(r)$ for subsets of points within windows reduced by 50 and 200 μm do not differ greatly from $G(r)$ for the whole sample.

Whilst it was clear in sample RN1B that the nucleation pattern should be split into separate internal and edge nucleated bubble populations, the complexities of the point patterns sample 79VB2C means that such a straightforward distinction is not possible. Observation of the change in $G(r)$ for a narrowing of the window of observation away from the sample edge enables us to

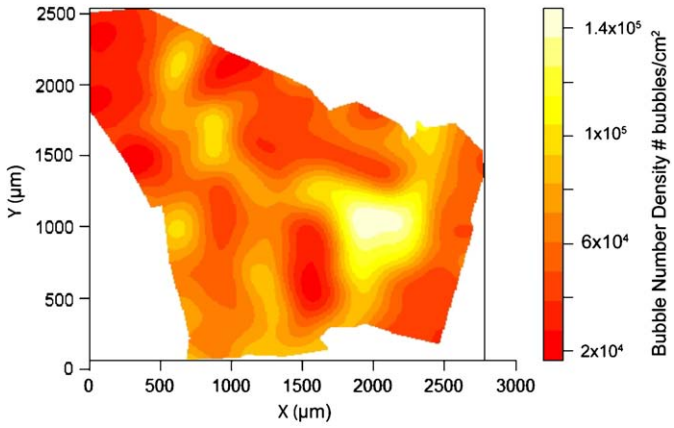

Fig. 8. Bubble number density plot for 79VB2C. Kernel size is 100.

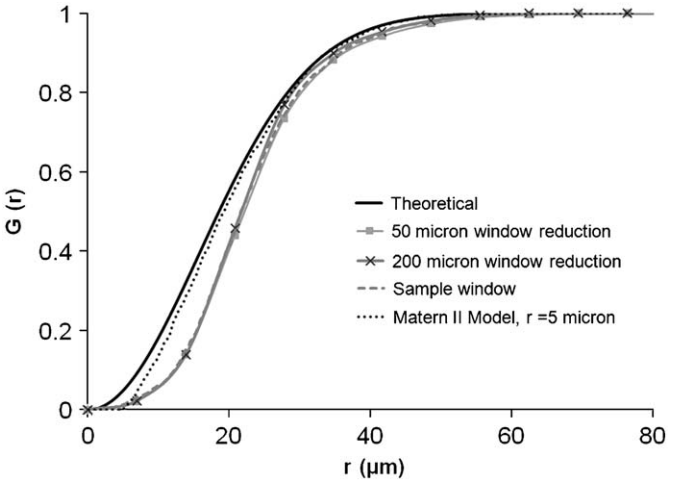

Fig. 9. $G(r)$ vs. $G_{Poiss}(r)$ for sample 79VB2C. Edge corrected nearest neighbor cumulative distributions, $G(r)$, for sample 79VB2C plotted against expected distribution from a Poisson distributed point pattern $G_{Poiss}(r)$ of same intensity. Black line is $G_{Poiss}(r)$, light grey line is $G(r)$ after reduced sample correction, and dashed dark grey line is $G(r)$ after Kaplan–Meier correction. Dashed black line is distribution derived from a Matern II model with minimum separation of 5 μm.

differentiate further between the two samples. From Fig. 9, we see that the spatial point pattern in sample 79VB2C is more regular than we would expect from a Poisson distribution with the same point intensity. Reducing the window of observation away from the sample edge has little effect on $G(r)$ even for a large reduction of 200 μm, (Fig. 9) suggesting that there is little difference in the spatial distribution of points at the sample edge and in the center and therefore that the controls on nucleation of bubbles close to the sample edge are similar to those for nucleation of "internal" bubbles. This suggests the bubbles in 79VB2C are not clearly separable into two distinct periods of nucleation, from two different mechanisms. More likely, the bubbles in 79VB2C represent heterogeneously nucleated bubbles, possibly from several nucleation pulses.

5. Summary

Application of the 2D spatial statistics model Spatstat to bubble nucleation experiments demonstrates a powerful method that will enable researchers to quantify bubble nucleation mechanisms and discriminate between samples with complex bubble textures. This model offers an improvement over simple visual recognition of bubble populations, used to discriminate between nucleation mechanisms qualitatively. Application of an eroding window can provide quantification of the length scales over which bubble populations change within the experiments, a clear step forward in quantification of complex textures, as seen in 79VB2C. Future applications could include quantification of multiple nucleation events by applying a combination of the eroding window technique with marked point processes. Bubbles resulting from separate nucleation events may be distinguishable by their size. By adding marks to each bubble according to a specified size range, the spatial characteristics of each bubble population may be analyzed separately, and in relation to other subsets. This could provide a way to estimate the timing and identify bubble number densities resulting from separate nucleation events within one experimental sample. Marked point process models could also be applied to crystal nucleation to understand the spatial dependence of crystal nucleation on prior nucleated crystals. Proper application of point process modeling could thus help transform our ability to interpret and apply experimental studies to volcanic processes.

Acknowledgements

An anonymous reviewer and Didier Laporte are thanked for their detailed reviews, which improved the final version of this manuscript.

Appendix A. Supporting Information

Supplementary data associated with this article can be found in the online version at doi:10.1016/j.cageo.2009.01.008.

References

Avrami, M., 1940. Kinetics of phase change I: general theory. Journal of Chemical Physics 7, 1103–1112.
Baddeley, A.J., 1998. Spatial sampling and censoring. In: Barndorff-Nielsen, O.E., Kendall, W.S., Van Lieshout, M.N.M. (Eds.), Stochastic Geometry: Likelihood and Computation. Chapman and Hall, London, pp. 37–78.
Baddeley, A., Turner, R., 2005. Spatstat: an R package for analyzing spatial point patterns. Journal of Statistical Software 12 (6), 1–42.
Burgisser, A., Gardner, J.E., 2004. Experimental constraints on degassing and permeability in volcanic conduit flow. Bulletin of Volcanology 67 (1), 42–56.
Cluzel, N., Laporte, D., Provost, A., Kannewischer, I., 2008. Kinetics of heterogeneous bubble nucleation in rhyolitic melts: implications for the number density of bubbles in volcanic conduits and for pumice textures. Contributions to Mineralogy and Petrology 156 (6), 745–763.
Cox, T.F., 1979. A method for mapping the dense and sparse regions of a forest stand. Applied Statistics 28, 14–19.
Diggle, P.J., Lange, N., Benes, F.M., 1991. Analysis of variance for replicated spatial point patterns in clinical neuroanatomy. Journal of American Statistical Association 86, 618–625.
Hirth, J.P., Pound, G.M., St. Pierre, G.R., 1970. Bubble nucleation. Metallurgical Transactions 1 (4), 939–945.
Hurwitz, S., Navon, O., 1994. Bubble nucleation in rhyolitic melts; experiments at high pressure, temperature, and water content. Earth and Planetary Science Letters 122 (3–4), 267–280.
Jerram, D.A., Cheadle, M.J., Hunter, R.H., Elliot, M.T., 1996. The spatial distribution of grains and crystals in rocks. Contributions to Mineralogy and Petrology 125, 60–74.
Johnson, W.A., Mehl, R.F., 1939. Reaction kinetics in processes of nucleation and growth. Transactions of the Metallurgical Society of American Institute of Mining, Metallurgical, and Petroleum Engineers (AIME 135), pp. 416–442.
Kolmogorov, A.N., 1937. Statistical theory of metals crystallization. Bulletin of the Academy of Science, USSR, Series Mathematics 3, 355–359.
Larsen, J.F., Denis, M.-H., Gardner, J.E., 2004. Experimental study of bubble coalescence in rhyolitic and phonolitic melts. Geochimica and Cosmochimica Acta 68 (2), 333–344.
Mangan, M., Sisson, T.W., 2000. Delayed, disequilibrium degassing in rhyolite magma; decompression experiments and implications for explosive volcanism. Earth and Planetary Science Letters 183 (3-4), 441–455.
Mongrain, J.C., Larsen, J.F., 2008. Rapid water exsolution, degassing, and bubble collapse observed experimentally in K-phonolite melts. Journal of Volcanology and Geothermal Research 173 (3–4), 178–184.
Mourtada-Bonnefoi, C.C., Laporte, D., 2004. Kinetics of bubble nucleation in a rhyolitic melt; an experimental study of the effect of ascent rate. Earth and Planetary Science Letters 218 (3–4), 521–537.
Peebles, P.J.E., 1974. The nature of the distribution of galaxies. Astronomy and Astrophysics 32, 197–202.
R Development Core Team, 2007. R: A language and environment for statistical computing. R Foundation for Statistical Computing, Vienna, Austria, 〈http://www.R-project.org〉.
Toramaru, A., 1989. Vesiculation process and bubble size distributions in ascending magmas with constant velocities. Journal of Geophysical Research, B, Solid Earth and Planets 94 (12), 17,523–17,542.